This is a repository copy of *Dynamic modelling of a servo self-pierce riveting (SPR) process*.

Article:

Original Article

Dynamic modelling of a servo self-pierce riveting (SPR) process

Daniel Tang[1,2] , **Mike Evans[1], Paul Briskham[1], Luca Susmel[3]** and **Neil Sims[2]**

Abstract

Self-pierce riveting (SPR) is a complex joining process where multiple layers of material are joined by creating a mechanical interlock via the simultaneous deformation of the inserted rivet and surrounding material. Due to the large number of variables which influence the resulting joint, finding the optimum process parameters has traditionally posed a challenge in the design of the process. Furthermore, there is a gap in knowledge regarding how changes made to the system may affect the produced joint. In this paper, a new system-level model of an inertia-based SPR system is proposed, consisting of a physics-based model of the riveting machine and an empirically-derived model of the joint. Model predictions are validated against extensive experimental data for multiple sets of input conditions, defined by the setting velocity, motor current limit and support frame type. The dynamics of the system and resulting head height of the joint are predicted to a high level of accuracy. Via a model-based case study, changes to the system are identified, which enable either the cycle time or energy consumption to be substantially reduced without compromising the overall quality of the produced joint. The predictive capabilities of the model may be leveraged to reduce the costs involved in the design and validation of SPR systems and processes.

Introduction

In the automotive industry, a major driving force behind the continued development and enhancement of joining techniques is the reduction of the weight of a vehicle, which has substantial benefits for both performance and fuel consumption.[1] This has led not only to the introduction of new materials in replacement of the mild steel traditionally used in the vehicle body, but also to the development of novel techniques that are better able to join said materials. Self-pierce riveting (SPR) is one such technique.

SPR is a mechanical joining method used commonly in the automotive industry in the assembly of panels, hoods and structural frames. It is a cold process in which a semi-tubular rivet is inserted into multiple layers of material to create a permanent joint. The deformation of the stack of material and the rivet is such that a mechanical interlock is formed during the insertion process. The rivet does not penetrate through the bottom-most layer of material. The four main steps of the rivet insertion process are illustrated in Figure 1. One approach used for forcing the punch against the die is via a 'squeeze'

type actuation, such as in a hydraulic SPR process where the components are pressed together at relatively low speed. Another approach is an inertia-based one, where the punch is attached to a flywheel mechanism to avoid the need for high actuation forces.

One of the challenges in the design of SPR processes is identifying the optimum process parameters for joining a given stack of material. A trial-and-error approach is often taken, in which many test samples may be used and discarded. Further complicating the matter is that the SPR system on the production line is unlikely to be the same as the designated test system. Differences often mean that additional testing would need to be performed

[1]Atlas Copco IAS UK Limited, Flintshire, UK
[2]Department of Mechanical Engineering, The University of Sheffield, Sheffield, UK
[3]Department of Civil and Structural Engineering, The University of Sheffield, Sheffield, UK

Corresponding author:
Daniel Tang, Department of Mechanical Engineering, The University of Sheffield, 36-38 Victoria Street, Sheffield S3 7QB, UK.
Email: dan.tang@atlascopco.com
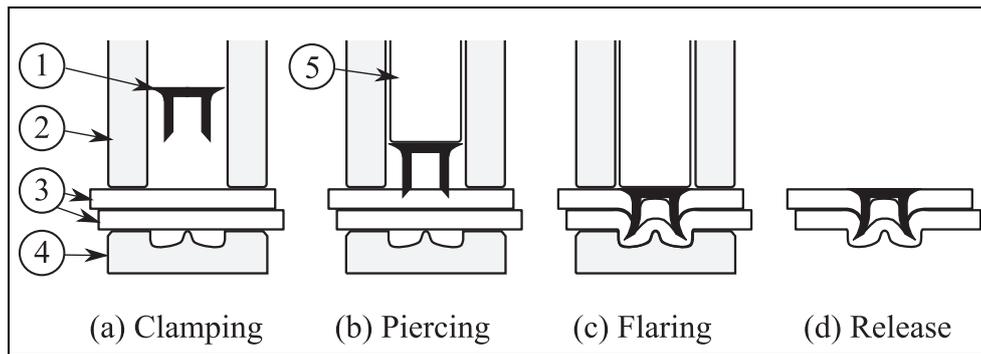
Figure 1. A cross-section view of the stages of the SPR process: (a) clamping of the material stack, (b) piercing of the top sheet of material, (c) flaring of the rivet shank to form the interlock, (d) release of the joint. Components are numbered as follows: (1) rivet, (2) blank holder, or clamp tube, (3) stack of material, (4) die, (5) punch.
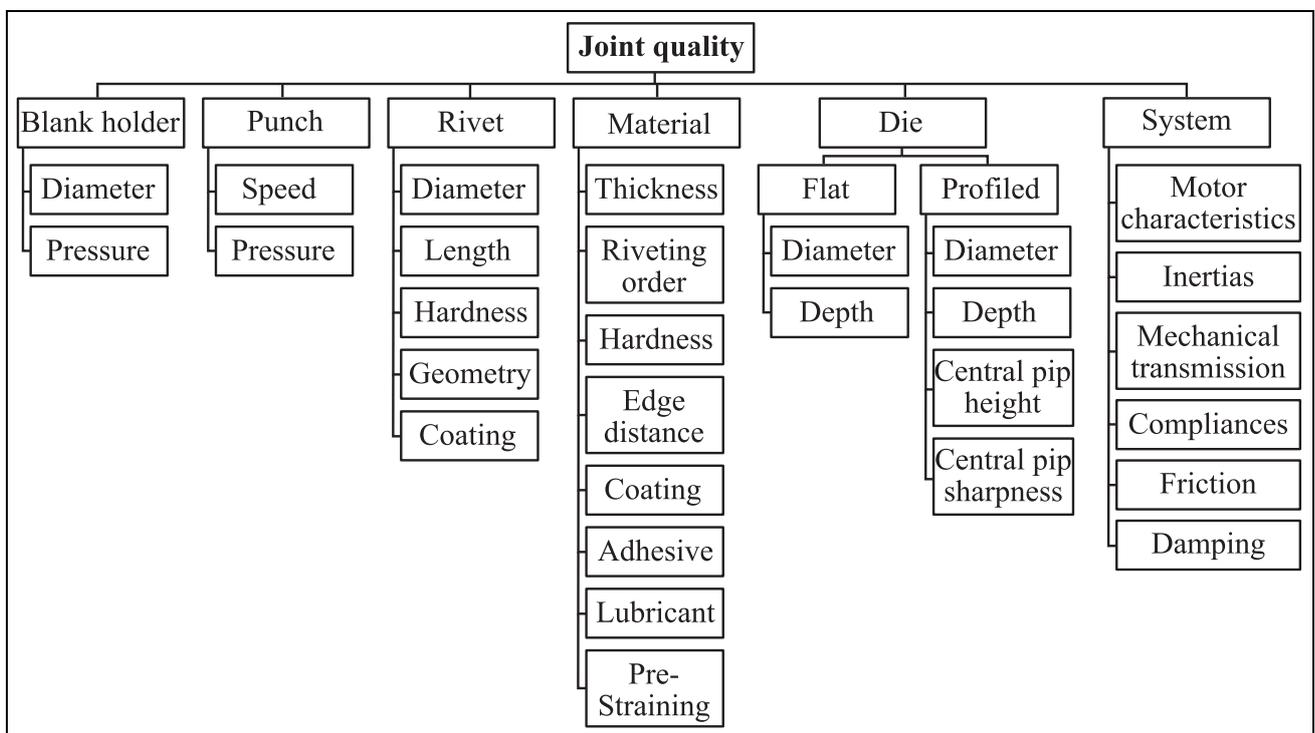
Figure 2. Factors that affect the SPR process, based on the work by Haque.[2]

at the test facilities of the production plant. All this can culminate in an enormous amount of testing, consumables and time. The need for a model-based approach is evident. A robust model which is able to predict the effects of changing the process inputs on the resulting joint would significantly reduce the experimental costs.

The number of process inputs that are known to influence the quality of the resulting joint is extensive, as illustrated in Figure 2, and this is a source of complexity for the modelling of the process.

In the published literature, finite element (FE) methods have been the main tool of choice in the simulation of SPR processes.[3–6] However, such works mostly deal with the interactions between the rivet, material and die, without accounting for the dynamics of the full riveting system.

Consideration of the full system would be a necessary step towards improving the model of the process. Existing work on the influence of process inputs on the SPR joint has tended to focus on either a single factor, such as the riveting velocity,[7–10] or a group of factors relating to the properties of the rivet, material and die.[11–13] Papers that have studied the sensitivity of the process via a model-based approach are centred around process parameters on the rivet-material level.[13–15] To date, the behaviour of the riveting machine and its influence on the joint is not fully understood.

FE simulations may provide useful insight on the deformation of the rivet and material, but challenges arise from difficulties in identifying suitable friction coefficients for all interfaces that come into contact, obtaining flow curves for materials and rivets, and defining the

damage model to handle large plastic deformations and fracture.[16] The computational cost poses another challenge when the number of runs is large. In the study by Fang et al.,[17] surrogate models were created from a FE model of the rivet insertion process to save time on a sensitivity analysis that looked into the effects of uncertain parameters in the model. However, the training of the surrogate models involved running 800 FE simulations, which is a considerable expense in itself.

Already a complex process, the introduction of system dynamics into a FE model of the joint would further increase the simulation time. In Liu et al.[18] the C-frame deflection was excluded from the main body of simulations based on trials where the introduction of a spring under the die incurred an increase in simulation time, but revealed no obvious effects on the results. Neglecting the wider system would perhaps make sense for simulations where the source of energy required for making the joint is not restricted. However, for inertia-based riveting systems, the energy matters since the larger proportion of the energy delivered to the joint is converted from the initial kinetic energy of the rivet setter. The amount of strain energy stored in the system during rivet insertion will also affect the energy deliverable to the joint.

Looking further afield, the effects of system dynamics on the workpiece is a more established topic in the simulation of forming, forging and press systems. Behrens et al.[19] used an 'offline-coupling' method to study the interactions between a forming machine and a workpiece. In Kroiß et al.,[20] the stiffnesses of a cold forging press and its tooling were included in the FE process simulation as linear spring elements. Groche et al.[21] used a compliance matrix in the modelling of a servo press to describe the position-dependent compliances of the system. Each of the aforementioned works acknowledged the need to account for the compliances in the machine

in order to obtain accurate simulation results. The same point equally applies to the SPR system, where the accuracy of the simulated outputs would also depend on the characterisation of the compliances in the full system, alongside other factors of influence.

The aim of the present contribution is to develop a system-level model of the SPR system which overcomes the above-mentioned shortfalls. In contrast to existing methods of modelling SPR, the current method adopts a systems approach to reduce the computational cost (compared to FE methods) and enable consideration of the mechanical, electrical and digital domains of the problem. Using the model, it is shown that design changes and performance improvements can be easily predicted for the SPR system. Among the outputs of the model, the head height and cycle time are two of the most important indicators used to assess the performance of the real SPR process, hence meaningful insights can be gathered from analyses made using the model, which also saves time by minimising the need for empirical tests.

The layout of the paper is as follows. The modelling of the system and the joint are described first. Then, the experimental setup is explained. This is followed by model validation via the comparison of simulated outputs to experimental data. A model-based case study is used to investigate the reduction of cycle time and alternatively the energy consumption of the SPR process. Finally, conclusions and ideas for further work are presented.

Modelling

Modelling of the system

An example inertia-based servo SPR system is illustrated in Figure 3, consisting of a permanent magnet synchronous motor, belt drive, planetary roller screw
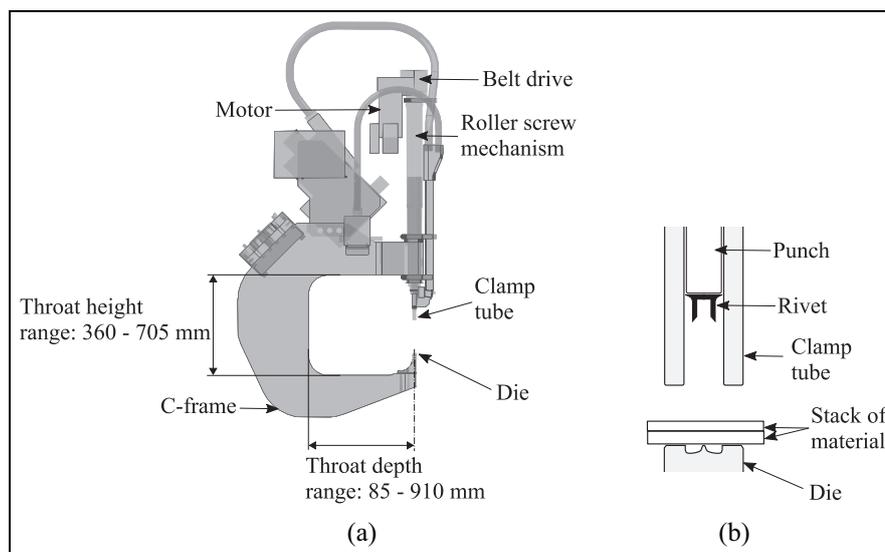
Figure 3. Schematic of a servo SPR system: (a) Full system. (b) Close-up of the riveting interface. Dimensions are shown for illustrative purposes only, indicating the approximate range for the height and depth of the opening between the upper and lower arms of existing C-frames. The opening affects the ability of the system to access joining locations on a structure or subassembly.
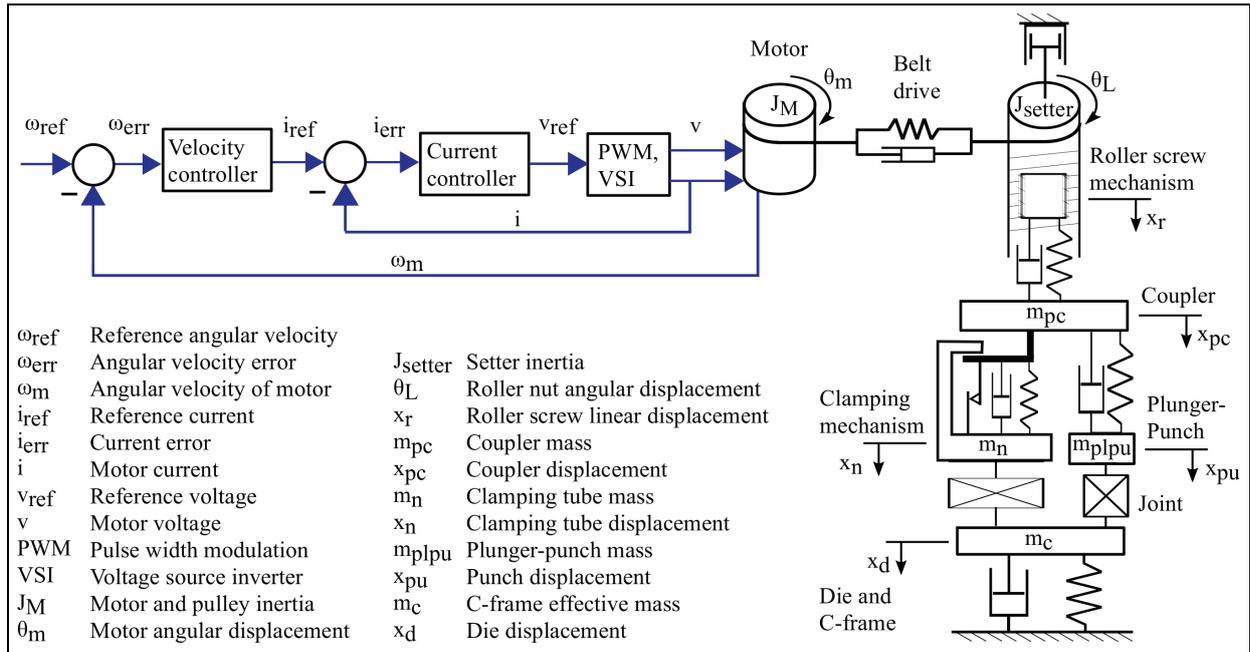
Figure 4. Lumped-parameter representation of the system.

mechanism (PRSM), clamping mechanism and C-frame. The core actuated mechanical subassembly is commonly referred to as the 'rivet setter'. The motor is controlled by a drive unit with an integrated programmable logic controller, not shown in the figure.

The PRSM is actuated by the motor via the belt drive, and transforms rotary motion into linear displacement of the punch, which is shielded inside the clamping mechanism. In a typical riveting operation, the punch and clamping mechanism are advanced towards the die and accelerated up to a predefined velocity, which determines the kinetic energy available for the riveting operation. The clamp tube holds the material stack against the die, and the rivet is driven into the material as the punch advances through the inside of the clamp tube. During this phase, the motor also applies a forward-driving torque to aid rivet insertion, which is determined by a predefined level for the motor current limit. At the end of rivet insertion the motor is reversed and the punch is retracted back to its start position. The punch and the die are in line and act on either side of the joint during rivet insertion. The C-frame provides the reaction force necessary for the forming of the joint.

A schematic of the lumped-parameter representation of the system is presented in Figure 4, with the control structure shown on the left side, and the mechanical system shown on the right.

The model of the system was developed from first principles and coded in MATLAB/Simulink. Values of parameters were either obtained from datasheets or experimentally identified. The full list of model parameters and values are provided in the supplemental material. The derivations for all equations in this paper are described in the work by Tang.[22]

Consider each subsystem in turn, starting with the motor:

$$J_M \ddot{\theta}_m = T_e - R_1{}^2 K_b \left(\theta_m - \frac{R_2}{R_1} \theta_L \right) - R_1^2 C_b \left(\dot{\theta}_m - \frac{R_2}{R_1} \dot{\theta}_L \right)$$

$$(1)$$

Where J_M is the total inertia of the motor and attached pulley, θ_m is angular displacement of the motor, T_e is the electromagnetic torque generated by the motor, R_1 and R_2 are the radii of the driving and driven pulleys respectively, K_b is the belt stiffness, θ_L is the angular displacement of the driven pulley, and C_b is the effective damping constant of the belt.

Next, consider the PRSM:

$$J_{setter} \ddot{\theta}_L = R_1 R_2 \left(K_b \left(\theta_m - \frac{R_2}{R_1} \theta_L \right) + C_b \left(\dot{\theta}_m - \frac{R_2}{R_1} \dot{\theta}_L \right) \right)$$
$$- \left(\frac{F_L P_h}{2\pi} + \text{sign}(\dot{\theta}_L) \frac{F_L D_0}{2} \mu_{prac} + B_r \dot{\theta}_L \right)$$

$$(2)$$

Here, J_{setter} is the inertia of the rivet setter, P_h is the lead of the PRSM, D_0 is the nominal diameter of the PRSM nut, μ_{prac} is the coefficient of Coulomb friction, and B_r is the viscous friction coefficient. The force F_L which is transmitted axially through the central shaft of the PRSM is described in terms of the effective stiffness (K_r) and damping (C_r) of the PRSM, the axial displacement of the roller assembly (x_r) and also that of the coupler (x_{pc}):

$$F_L = K_r (x_r - x_{pc}) + C_r (\dot{x}_r - \dot{x}_{pc}) \qquad (3)$$

The coupler links the output shaft of the PRSM to the punch, and plays a critical role in the generation of

the clamping force. Its governing equation is expressed in terms of the mass of the coupler (m_{pc}), the effective stiffness (K_{plpu}) and damping (C_{plpu}) of the plunger-punch subassembly, the displacement of the end of the punch (x_{pu}), and the force generated within the clamping mechanism (F_{clamp}):

$$m_{pc}\ddot{x}_{pc} = F_L - K_{plpu}(x_{pc} - x_{pu}) \\ - C_{plpu}(\dot{x}_{pc} - \dot{x}_{pu}) - F_{clamp} \tag{4}$$

Due to nonlinearities within the clamping mechanism such as the preloaded spring pack and hard stop, F_{clamp} takes the form of a piecewise function that is dependent on the relative motion between the coupler and the clamp tube, or $x_{pc} - x_n$. Letting $y = x_{pc} - x_n$, F_{clamp} can be expressed in terms of the coupler-clamp tube relative displacement (y), the stiffness (K_1) of the coil spring, the maximum distance between the coupler and hard stop (Z_1), the maximum available compression of the disc springs (Z_s), the stiffness (K_2) and damping (C_2) of the disc spring pack, the Coulomb friction in the disc spring pack (F_{c2}), the effective stiffness (K_3) and damping (C_3) of the hard stop contact:

$$F_{clamp} = \\ \begin{cases} K_1 y & \text{if } y < Z_1 - Z_s \\ F_1 + K_2(y - (Z_1 - Z_s)) + C_2\dot{y} + F_{c2}\,sign(\dot{y}) & \text{if } Z_1 - Z_s \leqslant y < Z_1 \\ F_1 + K_2 Z_s + K_3(y - Z_1) + C_3\dot{y} & \text{if } y \geqslant Z_1 \end{cases} \tag{5}$$

Where $F_1 = K_1(Z_1 - Z_s)$.

The three rows of equation (5) describe the three main stages of clamping in a riveting scenario:

1. Initially, a relatively low force to hold the material stack in place.
2. A significant rise in the clamping force to eliminate any gaps between the layers of material.
3. In the event of excessive displacement of the coupler towards the clamp tube, the hard stop comes into contact to limit further rivet insertion.

The force balance on the clamp tube is summarised as:

$$m_n \ddot{x}_n = F_{clamp} - r_{mat} \tag{6}$$

Where m_n is the mass of the clamp tube, $\ddot{x}_n$ is its acceleration and r_{mat} is the restoring force generated by the material stack under compression. Further details on the definition of r_{mat} are provided in Section 2.2.

The riveting force r is transmitted through the plunger-punch subassembly, the governing equation of which is expressed as:

$$m_{plpu}\ddot{x}_{pu} = K_{plpu}(x_{pc} - x_{pu}) + C_{plpu}(\dot{x}_{pc} - \dot{x}_{pu}) - r \tag{7}$$

Here, m_{plpu} is the mass of the plunger-punch subassembly. Details on the definition of r are given in Section 2.2.

The C-frame is modelled as single degree of freedom system consisting of an ideal mass-spring-damper arrangement. The dynamics of the C-frame are described in terms of the deflection between its upper and lower arms (x_d) and the restoring forces generated by the joint:

$$m_c \ddot{x}_d = r + r_{mat} - K_c x_d - C_c \dot{x}_d \tag{8}$$

Where m_c, K_c and C_c are the effective mass, stiffness and damping of the C-frame respectively.

Modelling of the joint

The approach taken in modelling the joint was based on the restoring force surface method,[23] an established technique used commonly in the identification of nonlinear systems. The method considers a system of interest as a black box or a nonlinear element, which generates a restoring force based on the displacement and velocity across that element.

The application of the restoring force method to SPR led to the representation of the joint as two distinct black-box models, in order to distinguish the dynamics of the rivet-material interaction and that of the material stack under clamping, away from the immediate rivet insertion zone. The simplification of the rivet insertion process is illustrated in Figure 5. Figure 5(a) shows a partially formed joint with components of the system that are in direct contact with the joint. The forces (i.e. r and r_{mat}) acting on the joint are noted in Figure 5(b). In Figure 5(c) the joint is visualised as two separate nonlinear elements: one
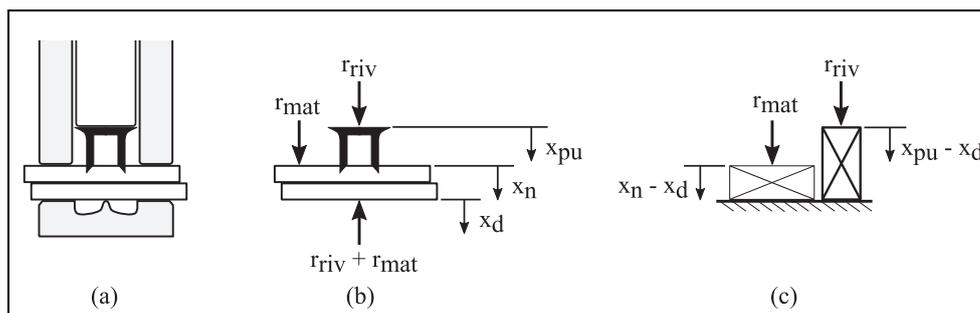
Figure 5. (a) Cross section view of the components in direct contact with a partially formed joint. (b) Cross section view of the joint with labelled forces. (c) Simplified representation of the joint.
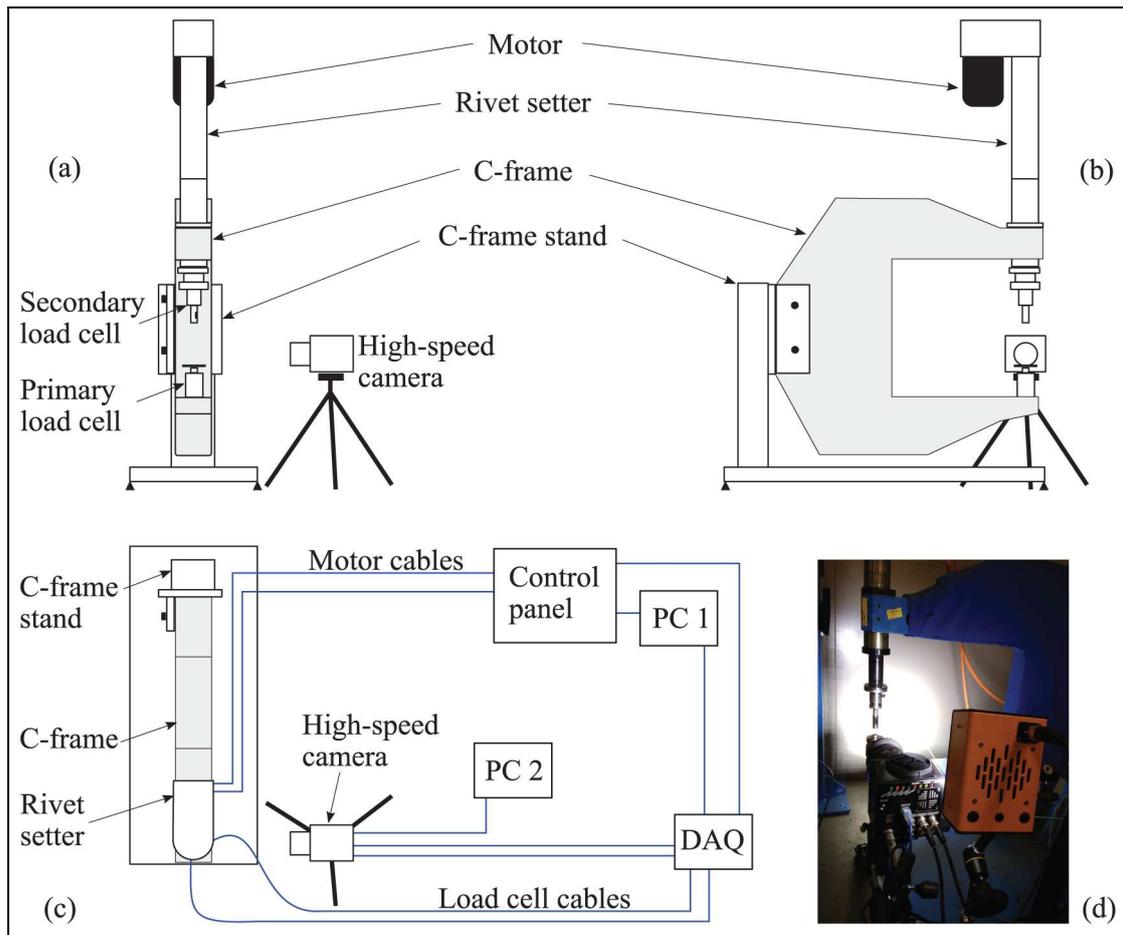
Figure 6. Front (a), side (b) and top down (c) views of the full experimental setup. (d) Photo of the high-speed camera, rivet setter and C-frame.

representing the material stack under compression by the clamp tube, and the other serving as a proxy for the rivet and the material into which it is inserted. The rivet-material interactions are encapsulated in the expression for r, and the behaviour of the material stack in r_{mat}. Compression of the material stack is represented by the relative displacement between the clamp tube and the die: $x_n - x_d$. Displacement of the rivet into the material is represented by the relative displacement between the punch and the die: $x_{pu} - x_d$.

As a measure of the depth of rivet insertion, an important output of the model was the head height of the joint, or the final position of the rivet head relative to the top surface of the top sheet of the riveted joint. This was calculated using:

$$Head\ height = Z_2 - (x_{pumax} - x_{nmax}) \qquad (9)$$

Where Z_2 is the internal stroke, a constant describing the distance between the end of the punch and the end of the clamp tube when the system is not under load, which must be traversed during rivet insertion. Maximum punch displacement (x_{pumax}) and clamp tube displacement (x_{nmax}) are taken from simulation of the riveting process at the point of maximum rivet

insertion. Head height equals zero when the punch end reaches the end of the clamp tube. Further displacement of the punch relative to the clamp tube leads to deeper rivet insertion (i.e. negative head height) and vice versa.

In order to identify the relationship between the forces and the relative displacements for a given rivet-material-die combination (or 'joint configuration'), an empirical approach was taken to obtain the relevant measurements from the actual riveting process. The experimental configuration is described in the following section.

Experimental setup

The test setup was developed strictly for the purposes of conducting the current research, and is illustrated in Figure 6. It consisted of a rivet setter and C-frame mounted on a stand, with two load cells for determining the individual components of the total process force: the punch force and the clamp force.

A high-speed camera was used to record the riveting process. Given that the rivet was not directly visible, the observed displacement of the punch relative to the die was used to estimate the extent of rivet insertion into the material. The head height of each joint, or the protrusion of the rivet head relative to the top surface of

Table 1. Details of the joint configurations used in testing.

Joint configuration	Rivet	Material and thickness
A	C-Rivet	1.5 mm RC5754 + 1.5 mm RC5754
B	K-Rivet	3 mm AC600 + 3 mm AC600

Table 2. Treatments used in testing. Five replicates were applied for each treatment.

Treatment	C-frame type	Setting velocity V (mm/s)	Motor current limit T (%)
1	1	150	100
2	1	150	150
3	1	250	100
4	1	250	150
5	2	150	100
6	2	150	150
7	2	250	100
8	2	250	150

the top layer of material, was measured using a dial test indicator.

The measurements taken during the rivet insertion event included the process forces, angular position and velocity of the motor, relative displacement between the punch and the die, relative displacement between the clamp tube and the die, and the motor current. Data acquisition was performed on the following data loggers at a sampling rate of 4 kHz:

- Bosch drive, housed inside the control panel
- Photron FASTCAM Mini UX100 high-speed camera
- National Instruments chassis and data acquisition modules

Experiments were run under laboratory conditions. The system was operated according to a predefined motion sequence, consisting of: advance, rivet insertion and retraction. The completion of a full sequence is referred to as a 'cycle'.

Two joint configurations were used in the test and are referred to as joint A and B from here onwards (see Table 1). All material stacks were prepared with square coupons of the indicated material measuring 40×40 mm in length and width.

A randomised two-level full factorial experiment design[24] was carried out, involving three factors: C-frame type, setting velocity and motor current limit. Two levels were defined per factor, and five replicates for each treatment. Table 2 shows the details of each treatment. All eight treatments were carried out for each joint configuration.

C-frame type 1 and 2 refer to the two types of C-frames used in the current study. Table 3 shows the key

Table 3. Key dimensions and effective stiffness of the C-frames used in testing.

C-frame type	Throat height (mm)	Throat depth (mm)	Effective stiffness (kN/mm)
1	400	450	14
2	360	300	29

dimensions as well as effective stiffness in the axis of rivet insertion.

Preliminary results and model identification

Important insights into the behaviour of the joint were gained from preliminary tests performed using C-frame 1 and joint A. Figure 7(a) shows the cross-section images of the joints made at various setting velocities, obtained by cutting through the centre of the joints using a circular saw. With increasing setting velocity the progressive nature of the rivet insertion and deformation can be clearly noted. Figure 7(b) shows the corresponding total force vs. relative displacement curves, where relative displacement represents the extent of rivet insertion. The loading phase of the individual curves appear to overlap, and can be said to lie on a common master curve, which suggests that the chosen joint configuration was not sensitive to the range of strain rates (i.e. relative velocities) seen in the test. The joint could therefore be characterised as a nonlinear stiffness using the observed force-displacement relationship.

The modelling of the joint required the characterisation of the force-displacement relationships for both the punch and clamp forces (r and r_{mat}). For the loading phase, the function for r was obtained via a polynomial fit to the loading part of the punch force vs. relative displacement data. The general form of r during the loading phase is given by:

$$r = f(x_{pu} - x_d) \tag{10}$$

For the unloading phase, the joint was modelled as a constant stiffness, which was a reasonable approximation to the true behaviour. The area enclosed within the loading and unloading curves is indicative of the amount of energy dissipated in the joint, that is, in the plastic deformation undergone by the rivet and material.

The behaviour of the material stack under direct compression of the clamp tube was approximated as a linear stiffness. r_{mat} was defined as:

$$r_{mat} = K_{mat}(x_n - x_d) \tag{11}$$

Where K_{mat} is the effective stiffness of the material stack, x_n is the displacement of the clamp tube and x_d is the displacement of the die. K_{mat} was estimated from the clamp force vs. clamp tube-die relative displacement data.
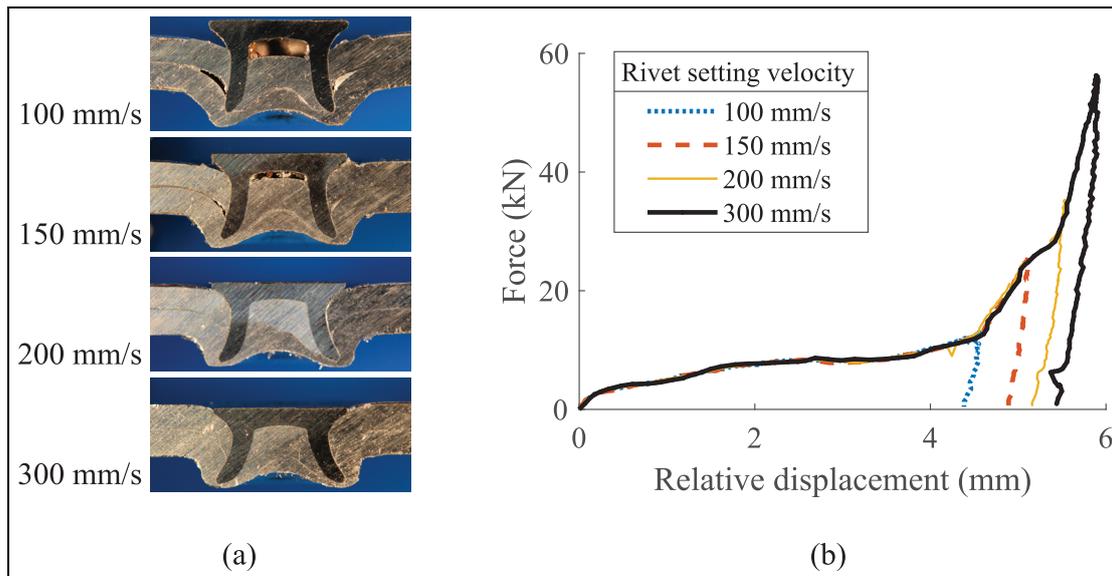
Figure 7. (a) Cross sections images of joint configuration A, made at the indicated setting velocities. (b) Total process force (sum of punch and clamp forces) vs. relative displacement data. Relative displacement represents the rivet insertion distance.

Since the definition of the restoring forces for the model of the joint was empirically-based, an associated disadvantage was that each unique combination of rivet, material or die would require a new set of experiments to be carried out in order to identify the model. On the other hand, the empirical model provided the necessary data exchange between the subsystems within the full model to enable predictions of the response of the system. The next section describes the validation of the model.

Model training and validation

For assessing the predictive performance of the full model, the acquired datasets corresponding to the eight treatments in Table 2 were divided into training and validation groups. Here, training refers to the process of generating a model of the joint from selected force vs. relative displacement data. Validation involved the comparison of experimental and simulated data for the following signals and metrics:

- Punch force – force transmitted directly through the rivet
- Clamp force – force transmitted through the material surrounding the rivet
- Relative displacement – extent of rivet insertion
- Relative velocity – rate of rivet insertion
- Head height – final state of the produced joint

The discrepancy between the simulated and experimental results was quantified using the normalised root mean square error (NRMSE), obtained by dividing the root mean square error by the range of the experimentally observed values of the associated signal.

Normalisation was necessary to enable comparisons between the performances of the different model variants of the joint, that is, models trained on different datasets. Selected validation cases for joint A are presented in this paper.

Figure 8 illustrates the steps involved in the training of the model of the joint and the validation of full model of the system. Figure 8(a) shows the selection of treatment 4 as the training dataset. The punch force versus punch-die relative displacement data from all five replicates are overlaid and curve fits of different polynomial orders are performed. These are assessed via the root mean square error (RMSE) as shown in Figure 8(b). Although a low RMSE is desirable, the visual inspection of how well the fitted curve captures the more nonlinear parts of the experimental data is also considered when it comes to selecting a suitable polynomial order. In this case an order of 10 gives a suitable model for the joint, as shown in Figure 8(c). Once the polynomial equation is obtained and implemented in the model of the full SPR system, the model is simulated eight times with the input conditions of each of the eight treatments. Subsequently the simulated results are compared to the experimental data for each treatment, as illustrated in Figure 8(d).

The model was trained on data from treatment 4. A polynomial of order 10 was fitted to define the function of the punch force: $r = -0.006x_{pd}^{10} + 0.175x_{pd}^{9} -2.080x_{pd}^{8} + 13.669x_{pd}^{7} - 54.278x_{pd}^{6} + 134.283x_{pd}^{5} -206.099x_{pd}^{4} + 189.342x_{pd}^{3} - 96.701x_{pd}^{2} + 26.909x_{pd}$, where

$$x_{pd} = x_{pu} - x_{d}.$$

The results of the subsequent validation against treatment 1 are shown in Figure 9. Excellent agreement is noted for all the signals.

1. Choose a treatment from which data will be used to train the model of the joint.

(a)   Treatments: 1   2   3   4   5   6   7   8
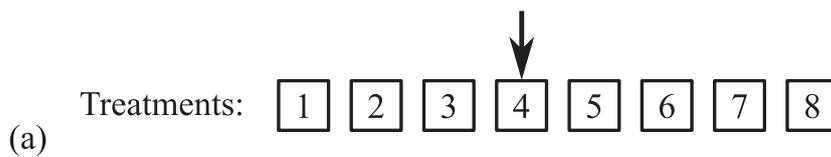
2. Train the model of the joint on Punch force vs. Punch-die relative displacement data, i.e. perform polynomial fit for multiple polynomial orders, then select suitable order based on RMSE.

(b)

(c)
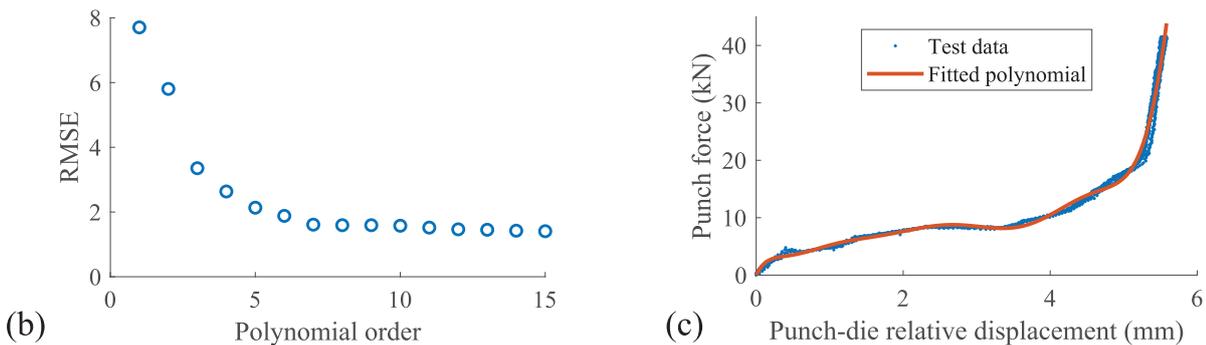
3. Run separate simulations with input conditions for each of the eight treatments.

4. Compare simulated result to each replicate dataset in a given treatment.

(d)
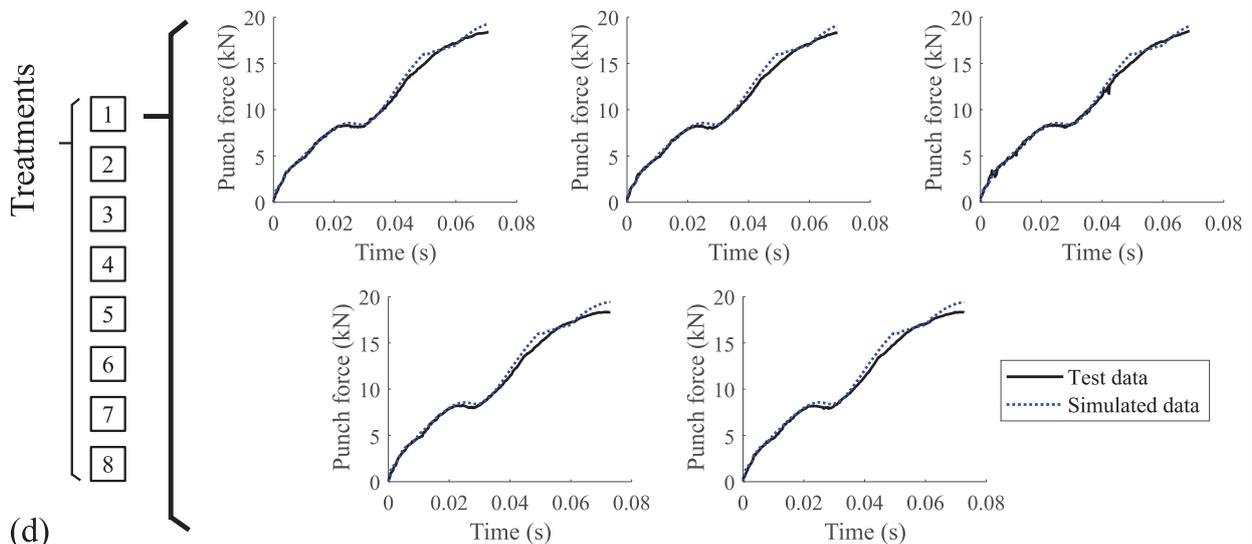
5. For each signal of interest, evaluate the NRMSE individually for each of the five replicates, then calculate the mean of the five NRMSE terms.

6. Perform steps 4 and 5 for all eight treatments.

Figure 8. Training and validation steps used to generate the model for the joint and evaluate the performance of the overall model of the system against test data. (a) Selection of a treatment to serve as the training dataset. (b) RMSE for various polynomial orders of the curve fit to the punch force vs. punch-die relative displacement data. (c) Selected curve fit to the punch force vs. punch-die relative displacement dataset, representing the restoring force model of the SPR joint. (d) Comparison of the simulated punch force against each individual replicate experimental dataset in treatment 1.
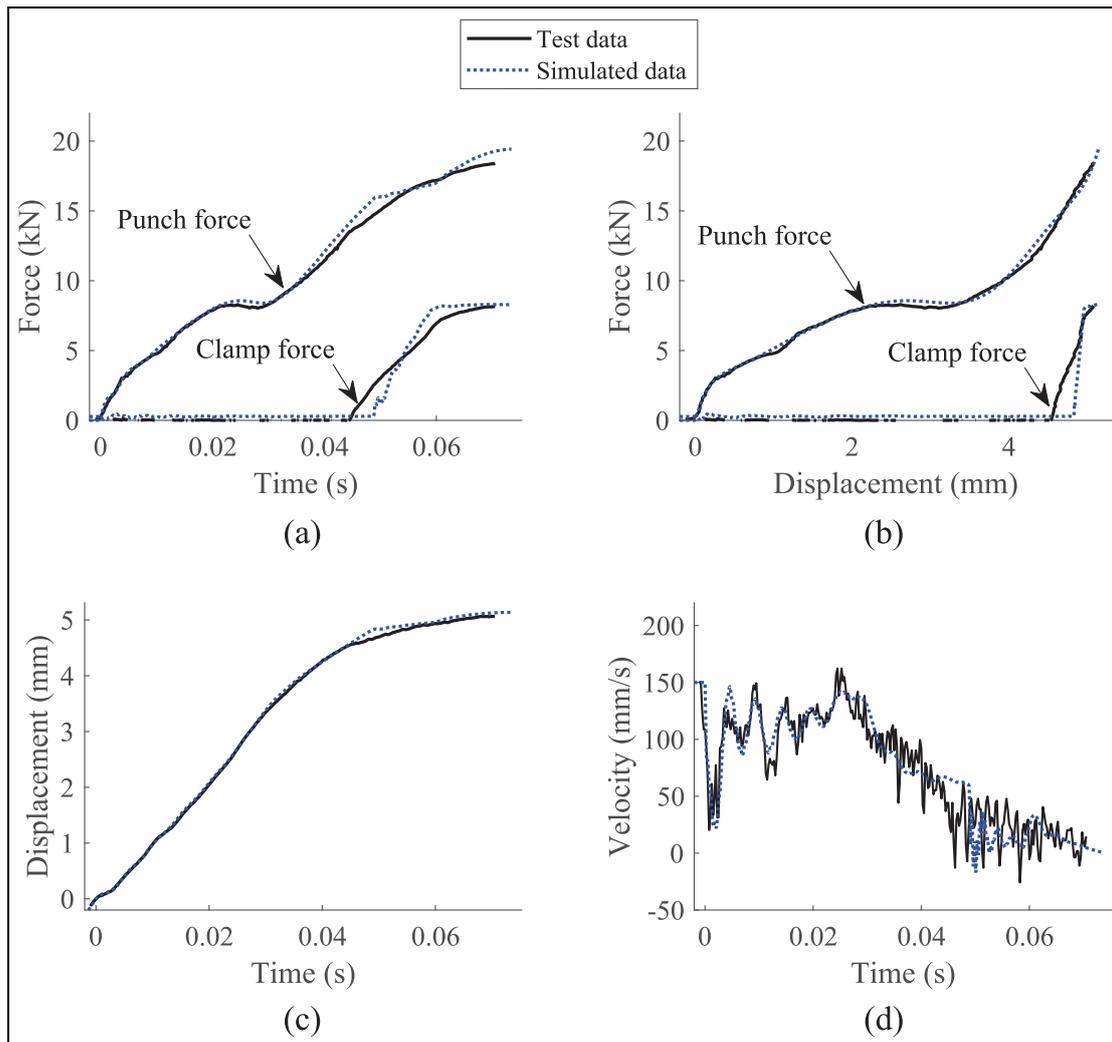
Figure 9. Comparison between experimental and simulated data. Training dataset: treatment 4. Validation dataset: treatment 1. (a) Punch and clamp force vs. time, (b) Punch and clamp force vs. relative displacement, (c) Relative displacement vs. time, (d) Relative velocity vs. time.

Figure 10(a) shows the resulting NRMSE values for the punch force when the model is validated across all the treatments. For each treatment labelled on the *y*-axis, the simulation output is validated against each individual replicate test result within the treatment. The individual bars in Figure 10(a) represent the mean NRMSE, and error bars are plotted at ±3 standard deviations either side of the mean.

It is seen that NRMSEs below 5% are achieved across all treatments. This is largely because in the case shown in Figure 10(a), the training dataset is associated with a setting velocity of 250 mm/s which provides good coverage of the force-displacement characteristic, thus it allows the restoring force to be computed mostly via interpolation when validating against the other treatments. A model with a more complete force-displacement curve is better suited to simulating a wider range of input conditions.

In Figure 10(b), predicted head heights are compared with the test results. Individual bars for the training and validation data represent the mean measured head height of all five repeat joints under a given treatment, the error bars are ±3 standard deviations from the mean. To put the accuracy of the simulation results into context, the absolute tolerances on the head height typically used in industry are indicated by the error bars on the x-axis with an upper limit of 0.3 mm and a lower limit of −0.5 mm,[7] which equates to a tolerance of ±0.4 mm about a nominal value of −0.1 mm. It can be seen that prediction errors of within ±0.25 mm are obtained across all the treatments. Although this exceeds the standard deviation of the experimental measurements, it is well within the tolerances used to judge joint quality in industry. The prediction accuracy is therefore considered to be high.

The results highlight the performance of the model in predicting the effects of making changes to the system, including the type of C-frame, setting velocity, as well as the motor current limit. The predictive accuracy is within the tolerances used by industry. This gives confidence in its usage for subsequent model-based investigations. In the current work, a case study to
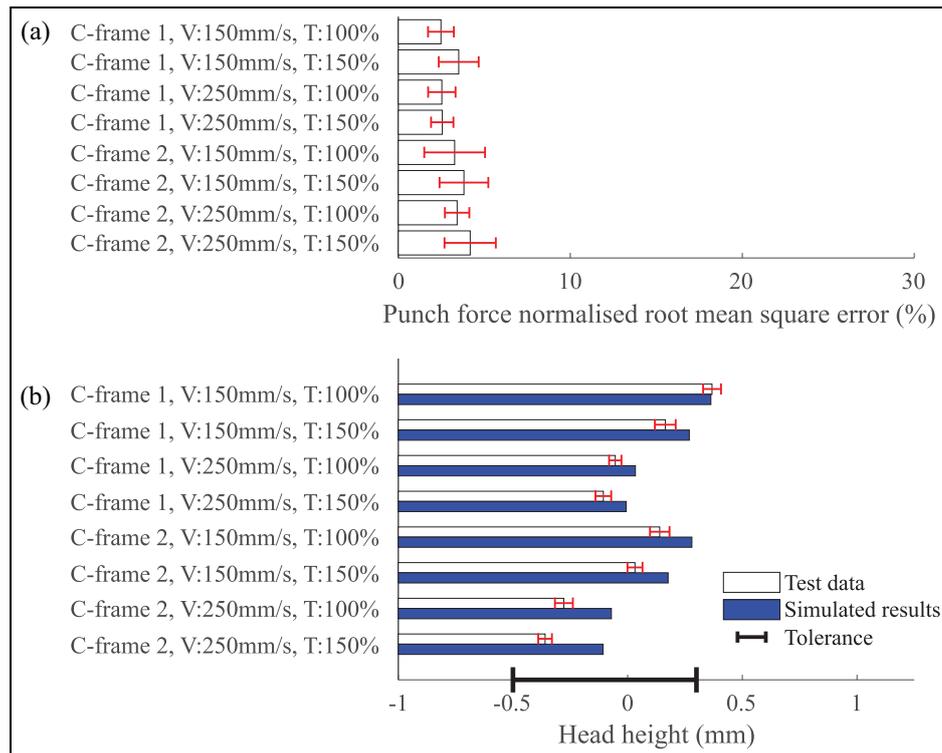
Figure 10. (a) Punch force NRMSE. V and T denote the setting velocity and motor current limit respectively. Error bars show the repeatability based on three standard deviations for five duplicate tests. (b) Comparison between measured and predicted head heights. Error bars on training and validation data show the repeatability based on three standard deviations for five duplicate tests. The error bars on the x-axis denote the tolerance on acceptable head heights typically used in industry.

explore the cycle time and energy consumption of the SPR process is performed.

Numerical case study

Introduction

The cycle time of the SPR process refers to the total duration of the sequence of steps in creating a single joint, as visualised in Figure 1. On high-volume production lines in the automotive industry, even a small reduction in cycle time could have large implications for the overall productivity of the plant, assuming that the SPR process is on the critical path of the full production process. On the other hand, shortened cycle time can be associated with increased energy usage by the system. This case study aims to investigate how the cycle time or the energy consumption can be minimised via changes to the system.

Two scenarios are considered:

1. Assuming the SPR system is on the critical path, minimise cycle time to increase productivity.
2. Assuming the SPR system is not on the critical path, minimise energy usage to reduce costs.

Scenario 1: Minimise cycle time

The model of the SPR system was used to estimate the potential reductions in cycle time achievable by changing the process parameters: the C-frame stiffness, motor current limit, stroke offset and setting velocity. Stroke offset refers to the distance between the end of the clamping mechanism and the workpiece, prior to the start of a riveting sequence. A smaller offset reduces the travel distance of the punch, whereas a larger offset facilitates access to joining locations.

Test cases were set up with joint A as the chosen joint configuration. Two levels of the motor current limit, three C-frame types corresponding to distinctive stiffness levels, and three levels for the stroke offset were defined. The chosen levels were representative of the range of values for real systems in the field.

In every case, the primary goal preceding that of cycle time minimisation was achieving a flush head height, that is, minimising the absolute head height. Hence, an optimisation problem was formulated to determine the setting velocity that would produce a flush head height:

Objective : Minimise|Head Height|

Constraint : $0 <$ Setting Velocity $< 400\text{mm/s}$

Where head height was calculated using equation (9).

The setting velocity was chosen as the only design variable, on which an upper limit constraint of 400 mm/s was placed, corresponding to the operating limit on the test system. The optimisation algorithm was based on golden section search and parabolic interpolation.[25]
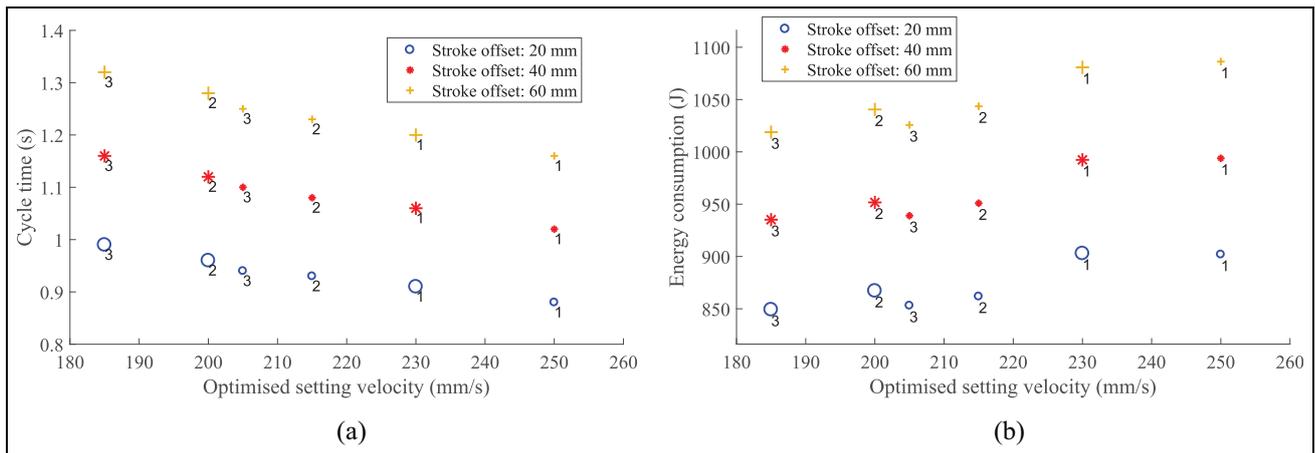
Figure 11. (a) Predicted cycle time vs. setting velocity optimised to achieve a flush head height. (b) Predicted energy consumption vs. setting velocity optimised to achieve a flush head height. Marker size represents the level of the motor current limit during rivet insertion, small: 50% limit, large: 100% limit. Marker labels denote the type of C-frame: 1, 2, and 3 correspond to C-frames with effective stiffness values of 14, 29 and 44 kN/mm respectively.

The model-predicted results for the setting velocity and cycle time are illustrated in Figure 11(a).

The stroke offset has by far the largest influence on the cycle time. Reducing the stroke offset from 60 to 40 mm gives an average cycle time reduction of 12%. Likewise, changing the stroke offset from 40 to 20 mm yields an average of 14% reduction in cycle time. Existing system configurations with large stroke offsets have potential for significant reductions in cycle time by shortening the stroke offset where practical.

For a given stroke offset, the cycle time appears to be closely related to the setting velocity: the higher the velocity, the shorter the cycle time. A lower motor current limit requires an accordingly higher setting velocity in order to produce a flush head height in the joint. Similarly, a more compliant C-frame requires an increase in the setting velocity, and vice versa.

With a view to reduce the cycle time, the problem is equivalent to maximising the setting velocity without compromising the head height of the resulting joint. This is attainable by selecting a C-frame of lower stiffness and reducing the motor current limit. Figure 11(a) shows that for a stroke offset of 20 mm, switching from C-frame 3 to 1 and changing the motor current limit from 100% to 50% would enable the setting velocity to be increased from 185 to 250 mm/s, resulting in a 10% reduction in cycle time. This could constitute a significant improvement in high-volume production scenarios.

Scenario 2: Minimise energy consumption

In this scenario, the primary concern was the energy usage of the system rather than the cycle time. The test cases from scenario 1 were equally applicable for scenario 2, except the problem was reframed to identify the configuration which yielded the lowest energy expenditure per cycle.

The total electrical energy consumed by the modelled system over a riveting cycle was computed from the time integral of the DC bus power. It was assumed that no energy was recovered from the braking phases of the motion, in accordance with the configuration of the real system. The predicted energy consumption is presented in Figure 11(b).

The results suggest that shortening the stroke offset is an effective way to reduce energy usage. Decreasing the stroke offset from 60 to 40 mm yields an average reduction of 8% in the energy usage, and from 40 to 20 mm the reduction is 9%. For a fixed stroke offset, the test cases which have the most contrasting energy consumption are those at either end of the velocity scale, that is, between 185 and 250 mm/s, for which a difference of 6% in the energy usage is noted.

In the context of a large automotive plant, where the total number of SPR joints made may reach hundreds of millions per year, a reduction of 9% in the energy consumption of the SPR systems would have a non-trivial impact on the carbon footprint as well as the running costs of the facility. Although typically in high volume production, a shorter cycle time may be weighted more favourably than a lower energy consumption, a more energy-efficient approach may be preferred if the scheduling is such that the cycle time of the SPR system does not directly affect the wider manufacturing process.

Discussion

A number of aspects are worth further discussion.

First, in the case study, it should be noted that the configuration with the minimal cycle time was identified manually from the results, rather than running a second optimisation routine for the cycle time. The analysis was structured this way since the parameter combinations were well defined and limited in number. Across the

population of real production systems in the field the parameters of interest such as C-frame stiffness, stroke offset and motor current limits generally fall within specific bands rather than a continuous range. This is due to the reuse of standardised configurations, mechanical designs and software code. Consequently, the case associated with the minimal cycle time could be easily identified without the need for a second objective function.

Regarding the head height minimisation, the assumption was made that the joints made to a flush head height would also meet the joint quality criteria in terms of other quality indicators such as interlock and minimum remaining thickness (also known as *t*-min). This assumption was based on prior knowledge of the chosen joint configurations, in the experience of the industrial co-authors. During the design phase of any new joint, the rivet, material and die combination is chosen such that the produced joint would satisfy the quality specifications when the head height is in the range −0.5 and 0.3 mm, as defined by industry standard practice.[7] Five samples are made at each of the three head height levels: −0.5, 0 and 0.3 mm, to verify that the interlock and t-min remain within tolerance for each associated head height level, before confirming a particular joint configuration as valid. Therefore, in subsequent reproductions of the joint, if the head height is within tolerance then it implies that the overall joint quality is acceptable. Despite this assumption, future work could explore other indicators of joint quality.

The strength of the joint is outside the scope of the current work. A point to note is that in automotive applications SPR is commonly used with an adhesive between the material layers. The strength and energy absorption characteristics of the resulting joints are notably enhanced, since the adhesive layer covers a significantly larger area than the rivet and takes most of the load until failure.[26] This means that the load-bearing capabilities of individual SPR joints are not as critical in such applications. The introduction of adhesive before the riveting process would inevitably change the characteristic force profile of the joint; the behaviour of the adhesive layer may make the riveting process more sensitive to the setting velocity, as well as the ambient temperature among other factors. The characterisation of SPR joints made with adhesives would be an interesting avenue for further work.

The findings of the case study indicate that in order to maintain the peak process forces at the same level, the stiffness of the C-frame must be reduced in relation to the increase in the setting velocity. This is easily implemented in the model, but in practice, reducing the stiffness of a C-frame may involve targeted removal of material from the structure. The impact of such changes on the behaviour of the C-frame and also the quality of the produced joint may be another area for further work.

Having identified higher setting velocities as being beneficial in terms of reducing cycle time, the implications on the life of the equipment are also worth further investigation. While the test cases of interest are not predicted to generate larger process forces than the existing process, the increased setting velocities may affect the life of the belt drive, the roller screw mechanism and other subsystems involved in the actuation of the punch.

Conclusion

In this study, a physics-based model of a servo-SPR system has been created in MATLAB/Simulink. In contrast to the existing body of research on the modelling of the SPR process, which has focused primarily on the rivet-material interactions without accounting for the dynamics of the riveting machine, the current work combines an analytical and an empirical approach to model the riveting system and the SPR joint in a single simulation environment.

The full model has been validated by comparing the simulated responses against experimental results. The model is able to predict the effects of changing the setting velocity, the motor current limit and the stiffness of the C-frame on the responses of the system, as well as the head height of the resulting joint to a high level of accuracy. This enables a rapid and straightforward model-based approach to the optimisation of the process parameters, ensuring that a satisfactory rivet head height is achieved without extensive empirical tests.

The usefulness of the model has been further demonstrated in a model-based case study on minimising cycle time or energy consumption, without compromising the head height of the resulting joint. It is shown that the cycle time can be reduced by maximising the setting velocity and minimising the stroke offset, which could lead to significant improvements in productivity. Alternatively, the energy consumption may be substantially reduced by minimising the setting velocity and stroke offset. Further work will seek to validate the predicted energy consumption for the different system configurations.

This study serves as a springboard for further investigation into the sensitivities of the SPR process to its input parameters as well as hardware configurations. The effects of process parameters on the riveting process continue to be a gap in knowledge of the SPR technique and should be addressed via a comprehensive sensitivity analysis.

Declaration of conflicting interests

The author(s) declared no potential conflicts of interest with respect to the research, authorship, and/or publication of this article.

ORCID iDs

Daniel Tang [iD] https://orcid.org/0000-0003-3358-4228
Luca Susmel [iD] https://orcid.org/0000-0001-7753-9176
Neil Sims [iD] https://orcid.org/0000-0002-6292-6736

Supplemental material

Supplemental material for this article is available online.

References

1. Pagerit S, Sharer P and Rousseau A. Fuel economy sensitivity to vehicle mass for advanced vehicle powertrains. *SAE paper 2006-01-0665*, 2006.
2. Haque R. Quality of self-piercing riveting (SPR) joints from cross-sectional perspective: a review. *Arch Civil Mech Eng* 2018; 18: 83–93.
3. Bouchard P-O, Laurent T and Tollier L. Numerical modeling of self-pierce riveting—from riveting process modeling down to structural analysis. *J Mater Process Technol* 2008; 202: 290–300.
4. Casalino G, Rotondo A and Ludovico A. On the numerical modelling of the multiphysics self piercing riveting process based on the finite element technique. *Adv Eng Softw* 2008; 39: 787–795.
5. Porcaro R, Hanssen AG, Langseth M, et al. Self-piercing riveting process: an experimental and numerical investigation. *J Mater Process Technol* 2006; 171: 10–20.
6. Huang L, Moraes JFC, Sediako DG, et al. Finite-element and residual stress analysis of self-pierce riveting in dissimilar metal sheets. *J Manuf Sci Eng* 2017; 139: 021007.
7. Han L, Thornton M, Li D, et al. Effect of setting velocity on self-piercing riveting process and joint behaviour for automotive applications. *SAE paper 2010-01-0966*, 2010.
8. Li D, Han L, Chrysanthou A, , et alLi D, Han L, Chrysanthou A, et al. The effect of setting velocity on the static and fatigue strengths of self-piercing riveted joints for automotive applications. In: The minerals metals & materials society (ed.) *TMS 2014: 143rd annual meeting & exhibition*. Cham: Springer, 2014, pp.557–564.
9. Hahn O, Kraus C, Leuschen G, et al. Research in impulse joining of self-pierce riveting. In: *3rd international conference on high speed forming* (ed kleiner M), Dortmund, Germany, 11–12 march 2008, pp.173–180. Dortmund: institut für umformtechnik - technische universität dortmund.
10. Wang B, Hao C, Zhang J, et al. A new self-piercing riveting process and strength evaluation. *J Manuf Sci Eng* 2006; 128: 580–587.
11. Westgate SA, Doo R, Liebrecht F, et al. The development of lightweight self-piercing riveting equipment. *SAE paper 2001-01-0979*, 2001.
12. Fu M and Mallick PK. Effect of process variables on the static and fatigue properties of self-piercing riveted joints in aluminum alloy 5754. *SAE paper 2001-01-0825*, 2001.
13. Jäckel M, Falk T and Landgrebe D. Concept for further development of self-pierce riveting by using cyber physical systems. *Procedia CIRP* 2016; 44: 293–297.
14. Mucha J. A study of quality parameters and behaviour of self-piercing riveted aluminium sheets with different joining conditions. *Strojniški vestnik-J Mech Eng* 2011; 57: 323–333.
15. Liu Y, Li H, Zhao H, et al. Effects of the die parameters on the self-piercing riveting process. *Int J Adv Manuf Technol* 2019; 105: 3353–3368.
16. Li D, Chrysanthou A, Patel I, et al. Self-piercing Riveting-a review. *Int J Adv Manuf Technol* 2017; 92: 1777–1824.
17. Fang Y, Huang L, Zhan Z, et al. Effect analysis for the uncertain parameters on self-piercing riveting simulation model using Machine Learning model. *SAE paper 2020-01-0219*, 2020.
18. Liu Y, Han L, Zhao H, et al. Numerical modelling and experimental investigation of the riv-bonding process. *J Mater Process Technol* 2021; 288: 116914.
19. Behrens B-A, Bouguecha A, Krimm R, et al. Consideration of the machine influence on multistage sheet metal forming processes. In: Denkena B and Hollmann F (eds) *Process machine interactions*. Berlin: Springer-Verlag Berlin Heidelberg, 2013, pp.403–417.
20. Kroiß T, Engel U and Merklein M. Comprehensive approach for process modeling and optimization in cold forging considering interactions between process, tool and press. *J Mater Process Technol* 2013; 213: 1118–1127.
21. Groche P, Hoppe F and Sinz J. Stiffness of multipoint servo presses: mechanics vs. Control. *CIRP Annals* 2017; 66: 373–376.
22. Tang D. *Developing a mechatronic system model for self-pierce riveting SPR tools*. PhD Thesis, University of Sheffield, UK, 2019.
23. Masri SF and Caughey TK. A nonparametric identification technique for nonlinear dynamic problems. *J Appl Mech* 1979; 46: 433–447.
24. Antony J. *Design of experiments for engineers and scientists*. 1st ed. Oxford: Butterworth-Heinemann, 2003.
25. Forsythe GE, Moler CB and Malcolm MA. *Computer methods for mathematical computations*. Englewood Cliffs, NJ: Prentice-Hall, 1977.
26. Moroni F, Pirondi A and Kleiner F. Experimental analysis and comparison of the strength of simple and hybrid structural joints. *Int J Adhes Adhes* 2010; 30(5): 367–379.